Chapter 7: Couplings Between Changes in the Climate System and Biogeochemistry

Coordinating Lead Authors: Guy Brasseur, Kenneth Denman

Lead Authors: Amnat Chidthaisong, Philippe Ciais, Peter Cox, Robert Dickinson, Didier Hauglustaine, Christoph Heinze, Elisabeth Holland, Daniel Jacob, Ulrike Lohmann, Srikanthan Ramachandran, Pedro Leite da Silva Diaz, Steven Wofsy, Xiaoye Zhang

Contributing Authors: David Archer, Vivek Arora, John Austin, David Baker, Joe Berry, Richard Betts, Gordon Bonan, Philippe Bousquet, Josep Canadell, Deborah Clark, Martin Dameris, Franck Dentener, Davod Easterling, Veronika Eyring, Johann Feichter, Pierre Friedlingstein, Inez Fung, Sandro Fuzzi, Sunling Gong, Nicholas Gruber, Alex Guenther, Kevin Gurney, Ann Henderson-Sellers, Joanna House, Andy Jones, Chris Jones, Bernd Kärcher, Michio Kawamiya, Keith Lassey, Carolyn Leck, Julia Lee-Taylor, Corinne Le Quéré, Gordon McFiggans, Yadvinder Malhi, Kenneth Masarie, Surabi Menon, John B. Miller, Philippe Peylin, Andy Pitman, Johannes Quaas, Michael Raupach, Peter Rayner, Gregor Rehder, Ulf Riebesell, Christian Rödenbeck, Leon Rotstayn, Nigel Roulet, Chris Sabine, Martin Schultz, Michael Schulz, Steve Schwartz, Will Steffen, David Stevenson, Yuhong Tian, Kevin Trenberth, Oliver Wild, Liming Zhou.

Review Editors: Kansri Boonpragob, Martin Heimann, Mario Molina

Date of Draft: 5 March 2006

Notes: TSU compiled version

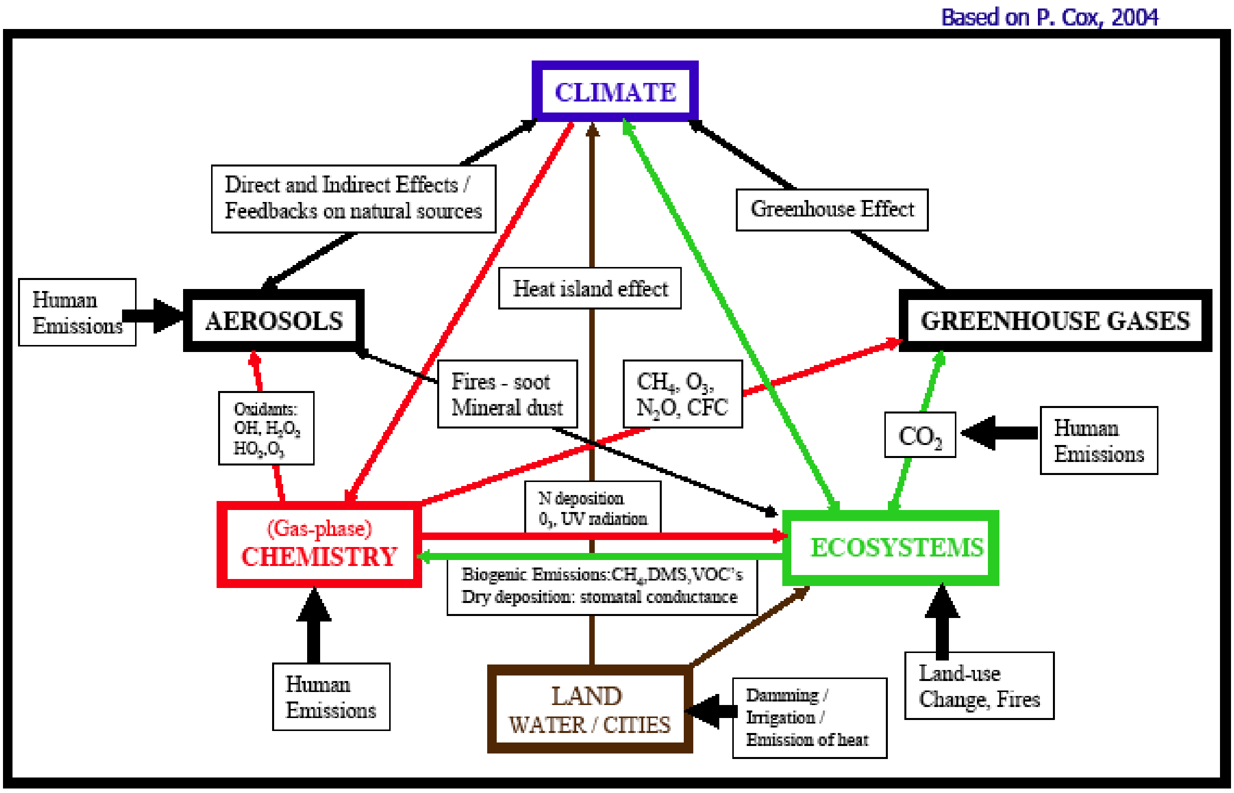

Figure 7.1.1. Schematic representation of some key interactions in the Earth system among climate, greenhouse gases, chemically reactive gases, aerosols and ecosystems. The effects of human activities on different elements of the Earth system are indicated.

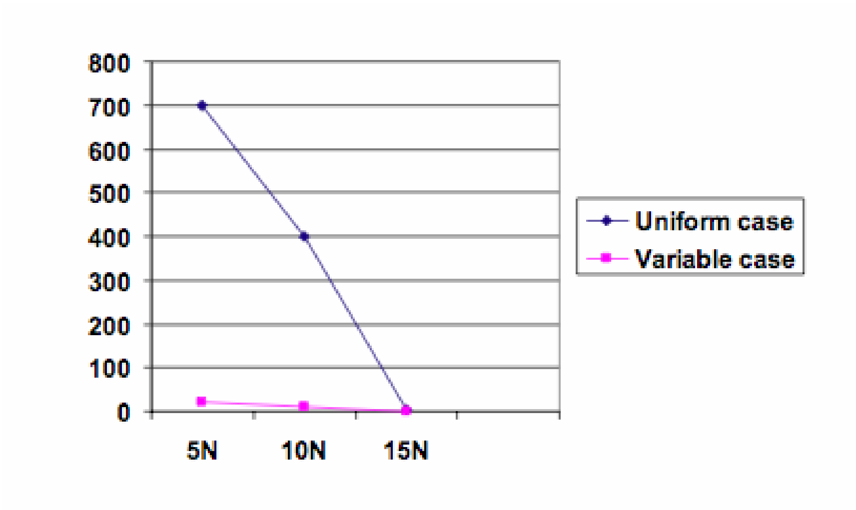

Figure 7.2.1. Redrawn from Figure 1d of Wang and Eltahir (2000) showing their modeled annual runoff over Africa north of the equator for a case with precipitation intensities modeled to be more realistic (the variable case) versus applied uniformly over the land area (the uniform case).

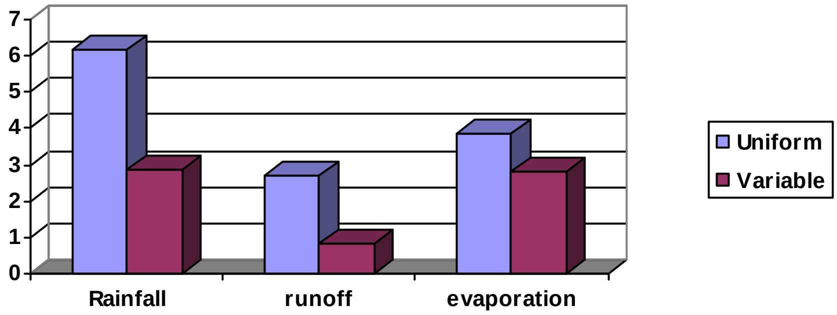

Figure 7.2.2. Derived from Table 3 of Hahmann (2003) showing averages of a climate model simulation over the equatorial Amazon (6°S to 6°N and 55°W to 66°W). Rainfall generated by the atmospheric model is distributed either uniformly over the basin or only over 10% of the area at any given time.

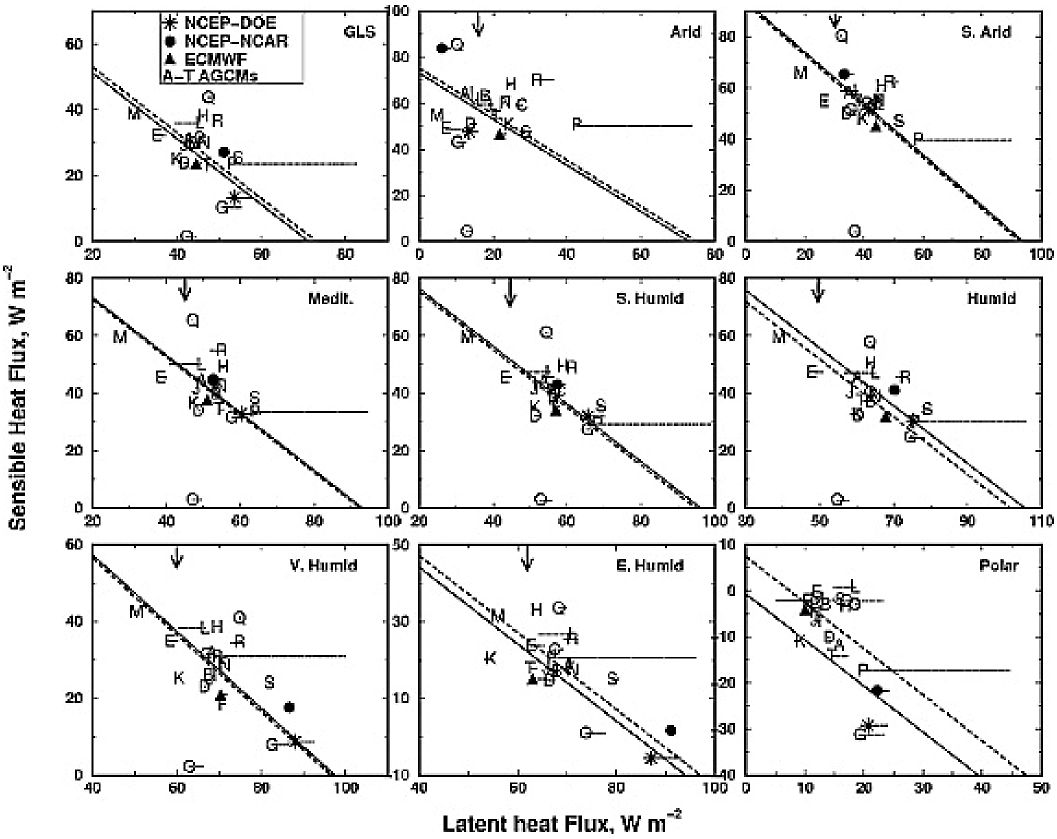

Figure 7.2.3. From Figure 1 of Henderson-Sellers et al. (2003), comparing the sensible and latent heat from 20 climate models with three sources of observational estimates.

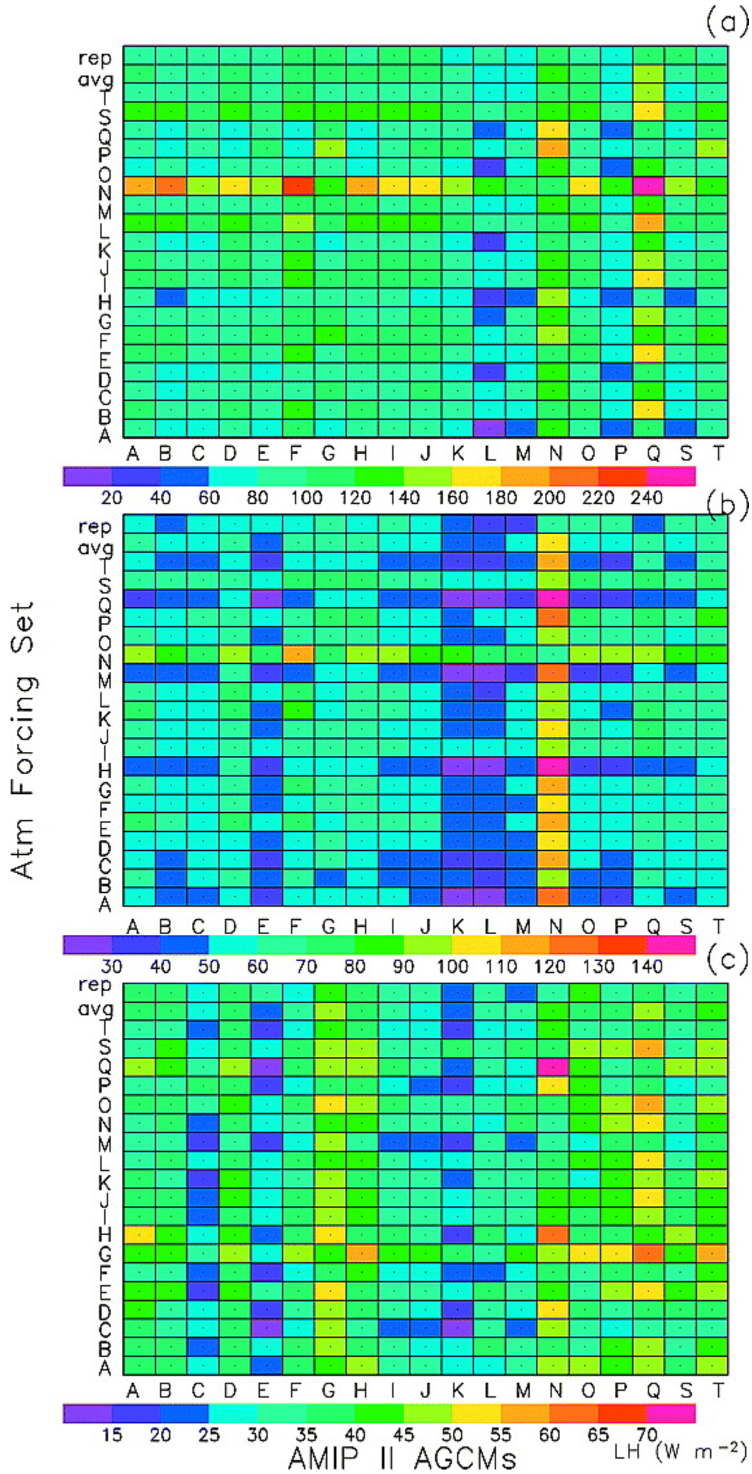

Figure 7.2.4. From Figure 2 in Irannejad et al. (2003), comparing the latent heat fluxes from 19 climate models for a) the Amazon basin (S. America), b) the Mississippi basin (N. America), and c) the Mackenzie basin (Canada). Each column represents the latent heat from a given land model when forced by the atmosphere of all the climate models. Each row represents the latent heat from all the land models when forced by the atmosphere of a single atmospheric model. The atmospheric forcing has been approximated by statistical fitting.

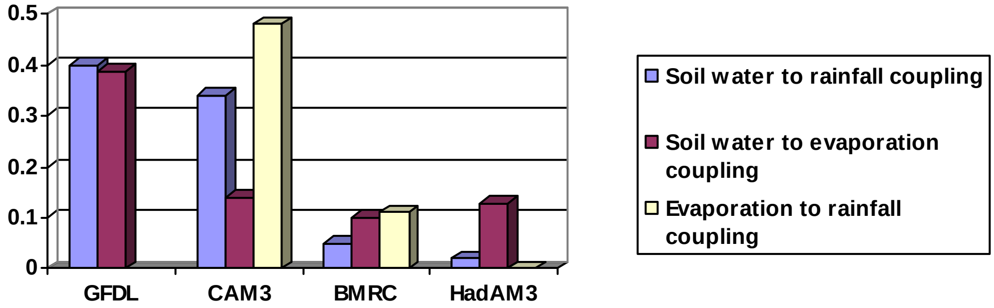

Figure 7.2.5. Derived from Table 1 of the GLACE study (Guo et al., 2006). In this study, different climate models are compared as to how strongly their soil water causes summer rainfall. This coupling is divided into how strongly soil water causes evaporation (including from plants), and how strongly this evaporation causes rainfall. The soil water-precipitation coupling is scaled by a factor of 10, and their two indices for evaporation to precipitation coupling are averaged. For simplicity, only 4 of the 12 models they analyze are shown.

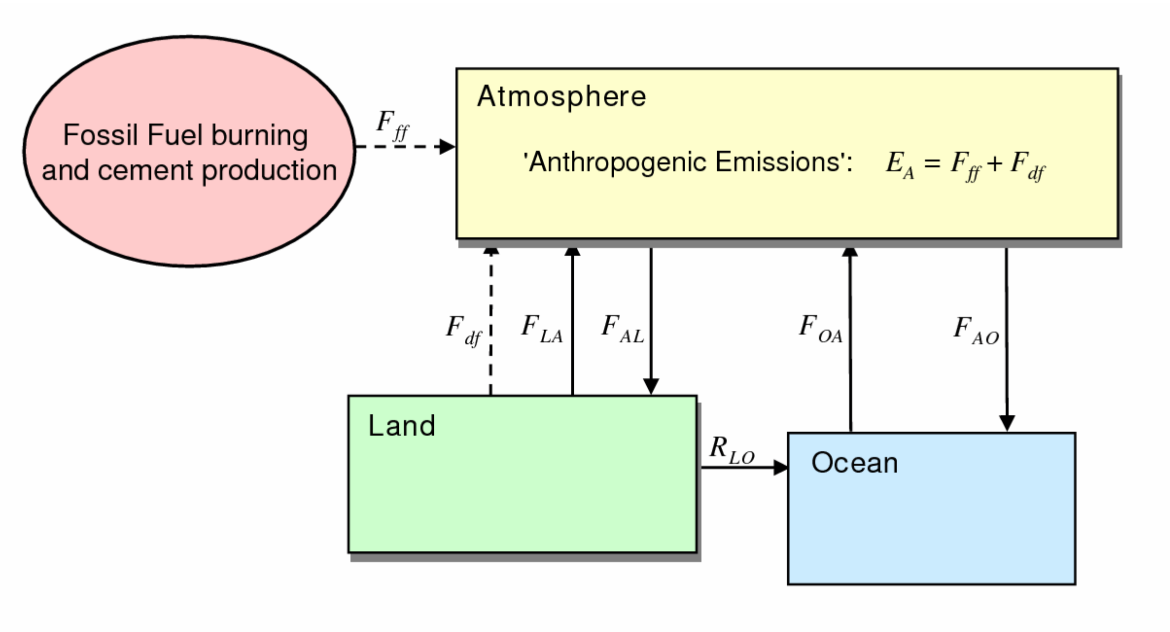

Figure 7.3.1. Schematic of the coupled Atmosphere-Land-Ocean carbon system. The ellipse represents new carbon released into the climate system from fossil fuel burning and cement production: F_{ff} represents the flux of CO_2 from these sources to the atmosphere (Gt-C) in a specified time period. F_{df} represents the direct flux of CO_2 to the atmosphere from deforestation. Therefore $F_{ff} + F_{df}$ (dashed arrows) represents total 'anthropogenic emissions' to the atmosphere in the specified time period. Other fluxes F_{ij} denote the total flux from basin ***i*** to basin ***j*** (e.g., F_{AO} represents the flux of carbon from the Atmosphere to the Ocean). R_{LO} denotes the total flux of carbon from Land to Ocean via rivers and runoff. For roughly 10,000 years prior to 1750, the carbon cycle is assumed to have been in equilibrium, with 'anthropogenic emissions' and the net flux of carbon into each reservoir all equal to zero. In the current changing climate, these quantities are all usually nonzero, and all other fluxes are assumed to be perturbed from their 'pre-industrial' equilibrium values, due to forcing by anthropogenic emissions, land use change, and climate change associated with human activities.

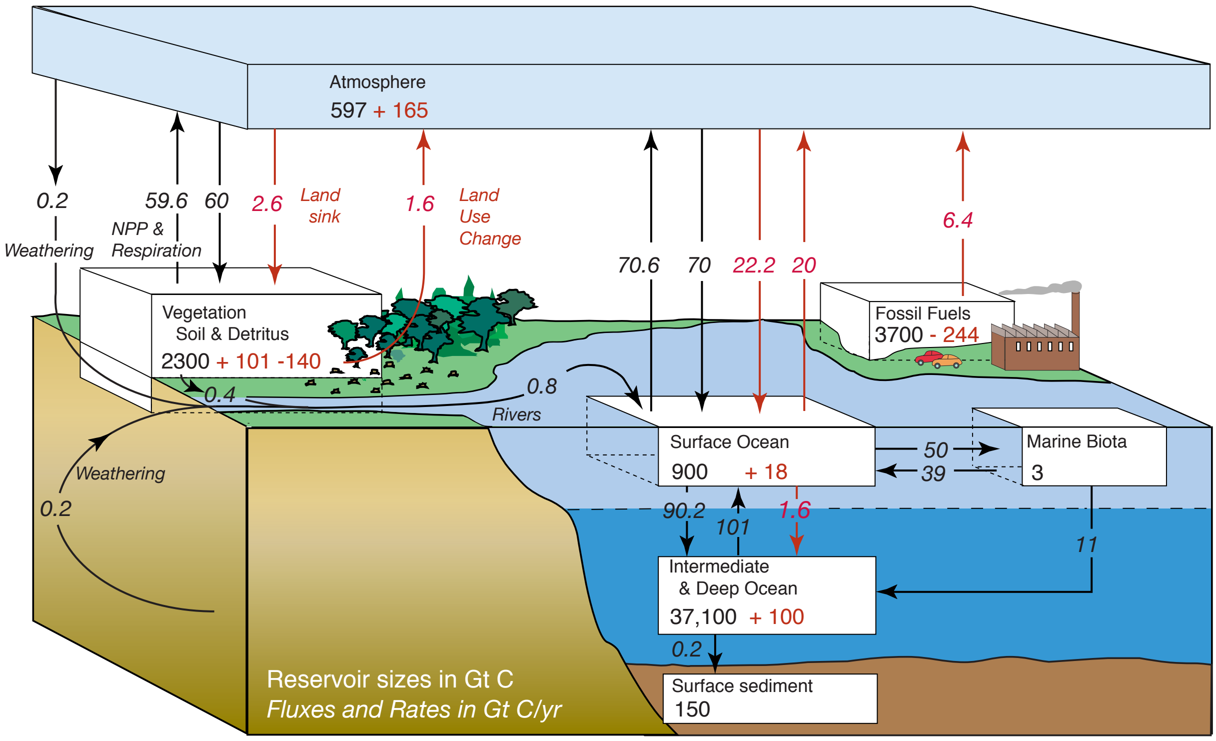

Figure 7.3.2. The global carbon (dioxide) cycle for the 1990s, showing main annual fluxes in GtC yr^{-1}: preindustrial 'natural' fluxes in black and 'anthropogenic' fluxes in red. Modified from Sarmiento and Gruber (2002), with changes in poolsizes from Sabine et al. (2004a): the flux of –140 GtC from the 'Vegetation, Soil & detritus' compartment represents the cumulative emissions from land use change. The net terrestrial loss of –39 GtC inferred from ocean storage requires a terrestrial biosphere sink of 101 GtC. Net anthropogenic exchanges with the atmosphere are from column 5 'AR4' in Table 7.3.1. Gross fluxes generally have uncertainties of more than 20% but fractional amounts have been retained to achieve overall balance when including estimates in fractions of GtC yr^{-1} for riverine transport, weathering, deep ocean burial, etc. NPP is net (terrestrial) primary production.

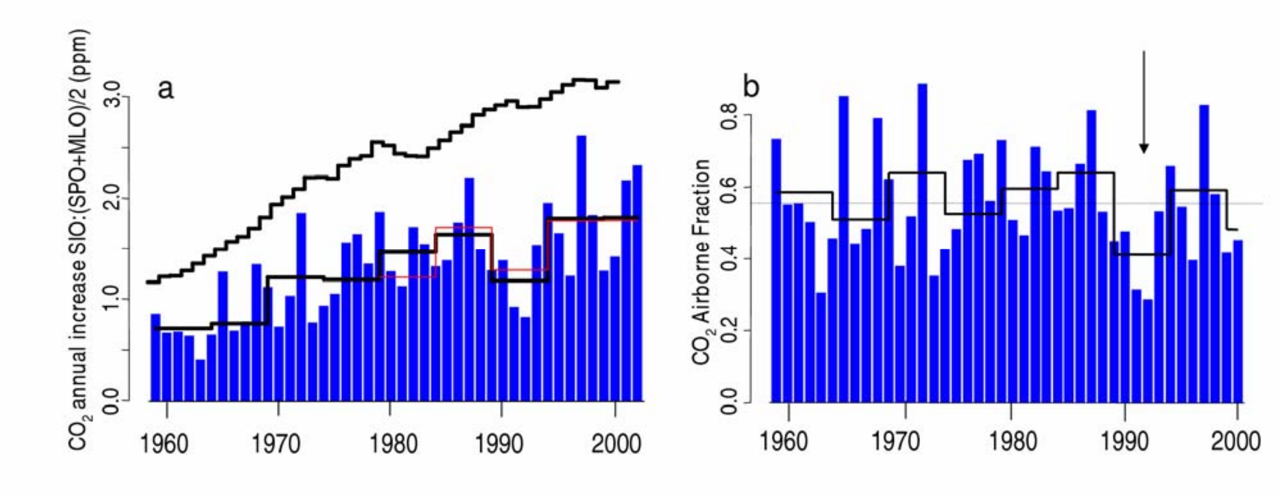

Figure 7.3.3. Atmospheric CO_2: (a) (l, –), *SIO data:* annual changes and 5-yr means of global CO_2 concentrations; (*upper* –): annual increases if 100% of fossil fuel emissions stayed in the atmosphere; and (–), *CMDL data*: 5-yr mean annual increases (1959–2003); (b) Fraction of fossil fuel emissions remaining in the atmosphere each year ("Airborne fraction", l), 5-yr mean (*line* –) (SIO data), and mean since 1958 (---). Note (↓) the anomalously low airborne fraction in the early 1990s. Will be updated via Ralph Keeling to include 2000–2004, which is slightly higher than the long term mean.

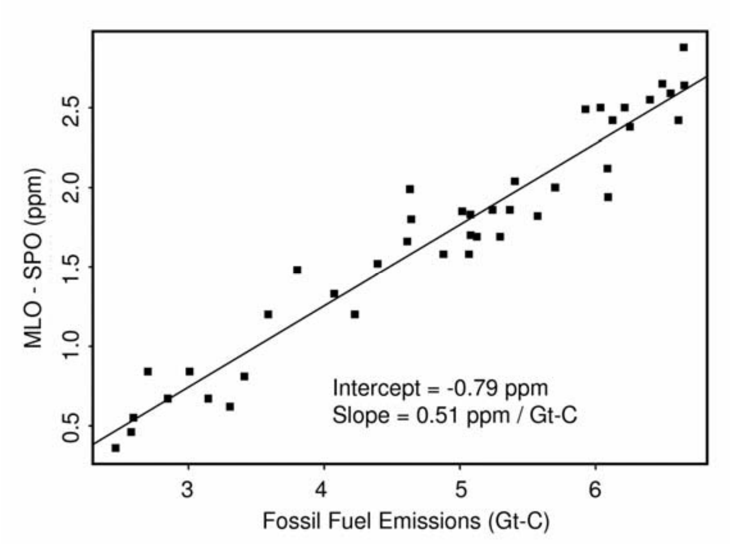

Figure 7.3.4. North-south CO_2 concentration difference, as indicated by MLO - SPO (ppm) , plotted against annual fossil fuel emission flux (Gt-C), 1959–2003.

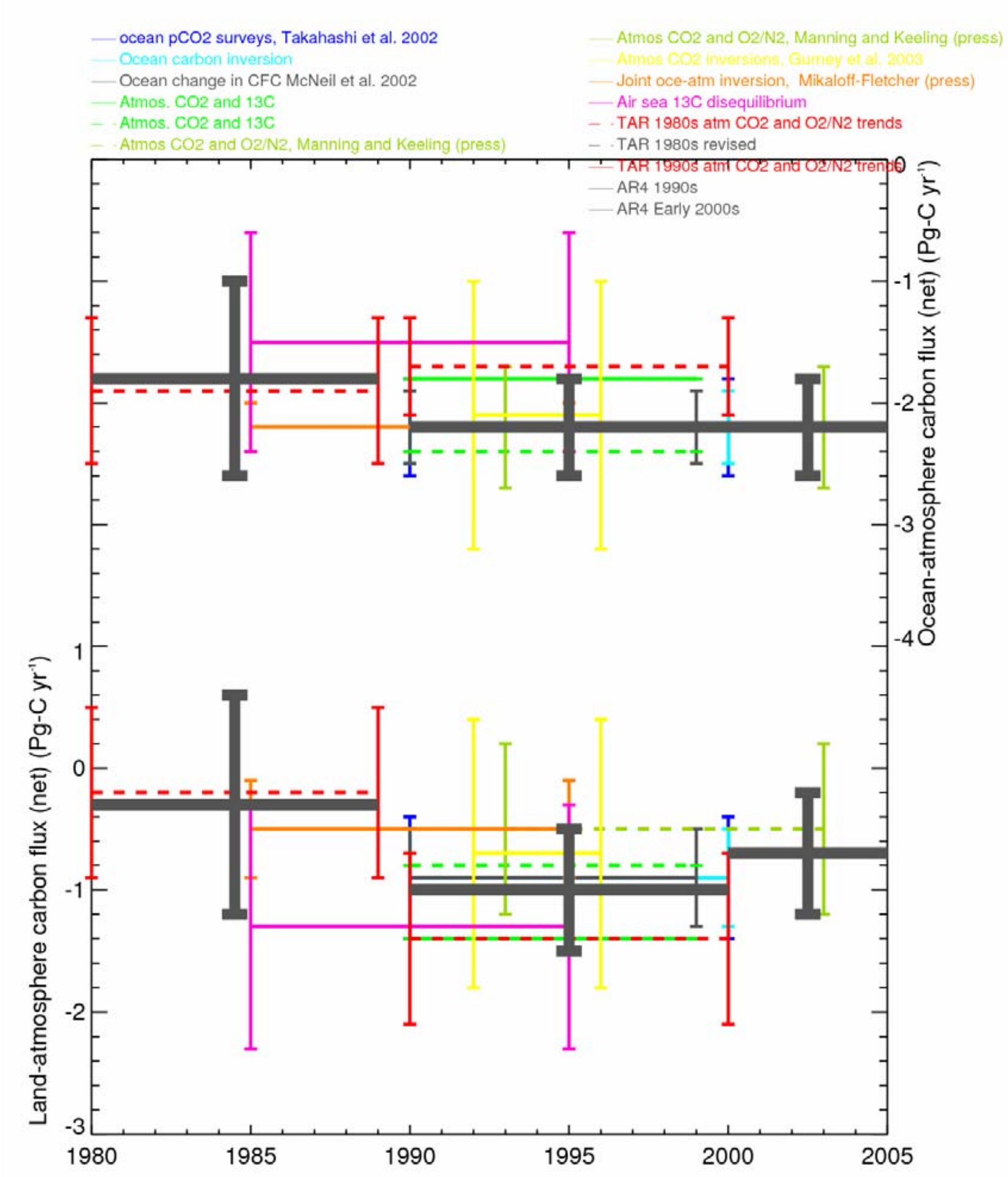

Figure 7.3.5. Individual estimates of the ocean-atmosphere flux reported in Chapter 5 and of the pertaining land-atmosphere required to close the global carbon budget equation. The grey thick lines are the revised budget estimates for the 1980's, the 1990's and the early 2000's respectively.

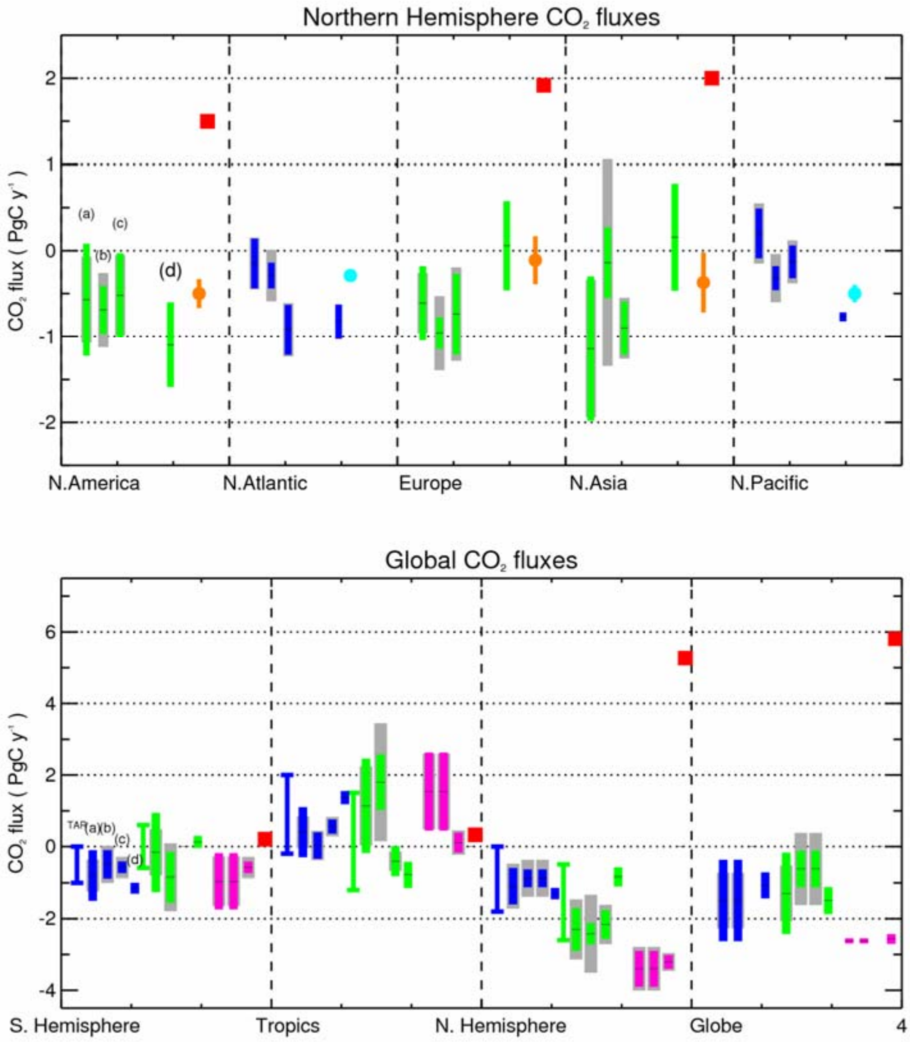

Figure 7.3.6. Regional ocean-atmosphere and land-atmosphere CO_2 fluxes from inversion ensembles and bottom-up studies. Inversion results all correspond to the period 1992–1996. Top Panel. Regional fluxes in the Northern Hemisphere. Bottom panel. Regional fluxes over the globe, grouped into three latitude bands. *Orange* = Bottom-up continental-level land-atmosphere flux estimates, (Pacala, et al., 2001) and (Kurz and Apps, 1999) for North America, (Janssens, et al., 2003) for Europe, and (Shvidenko and Nilsson, 2003) plus (Fang, et al., 2001) for North Asia (Asian Russia and China). *Cyan* = Bottom-up ocean basin level flux estimates (Takahashi, et al., 2002), *Blue* = ocean-atmosphere fluxes from inversion models, *Green* = land-atmosphere fluxes from inversion models, *Magenta* = land plus ocean inversion fluxes, *Red* = fossil fuel emissions. The mean flux of different inversion ensembles is reported with the random errrors and the range of bias due to different inversion settings within each ensemble. Error boxes show inversions random and systematic uncertainties. *Coloured error boxes* = average of 1-sigma Gaussian random errors returned by each member of the ensemble. *Grey error boxes* = spread of mean fluxes from inversions of the ensemble, with different settings. *TAR* = range of mean fluxes from Third Assessment Report (TAR, Chapter 3, Figure 3.5); **(a)** = (Gurney, et al., 2002) inversions using annual mean CO_2 observations with grey error from 16 transport models ; **(b)** = (Gurney, et al., 2003) inversions using monthly CO_2 observations with grey error from 13 transport models ; **(c)** = (Peylin, et al., 2005) inversions with grey error from 3 transport models times 3 set of large regions, times 3 inversion settings ; **(d)** = (Rödenbeck, et al., 2003a) inversions where the fluxes are solved on the model grid, using monthly flask data, with the grey error from their different sensitivity inversions.

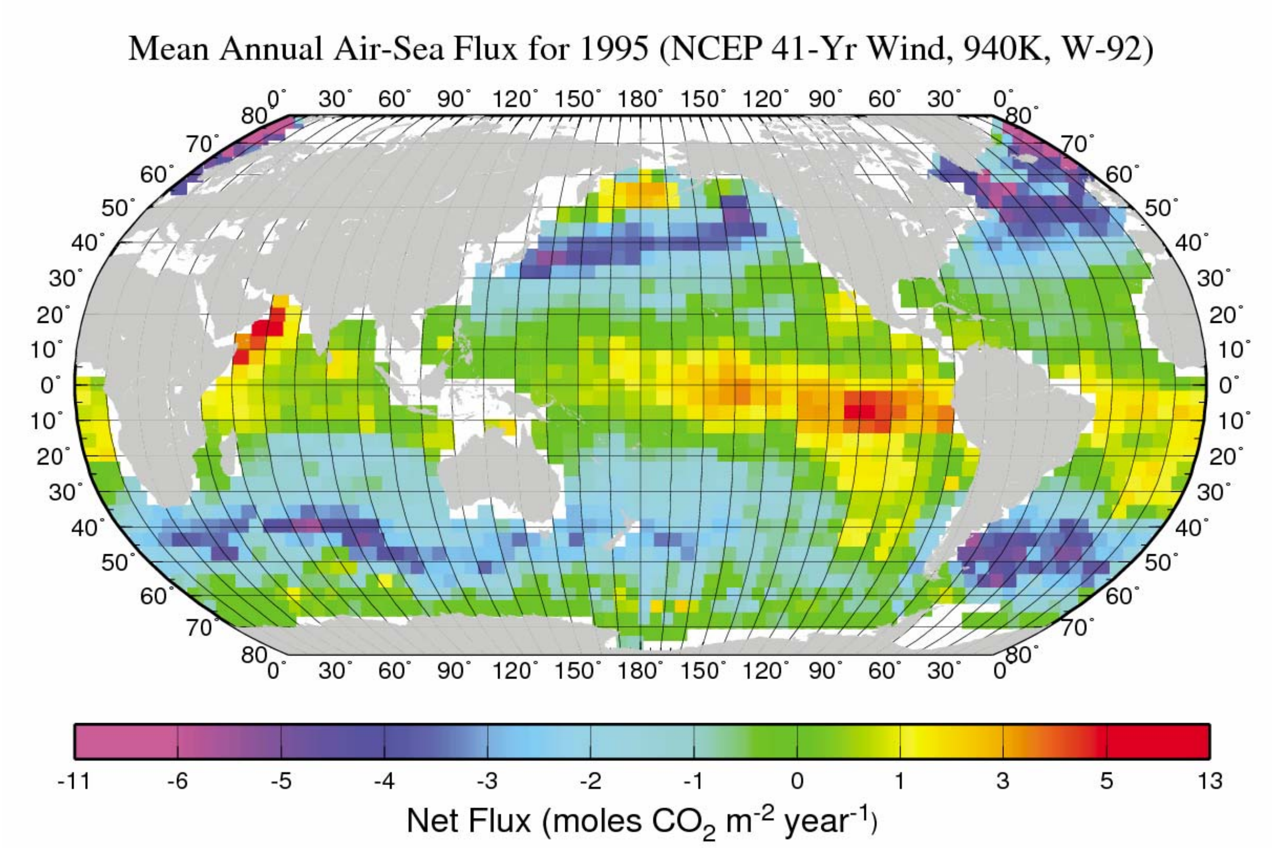

Figure 7.3.7. The 5° x 5° estimates of air-sea flux of CO_2 shown here (from Takahashi et al., 2002) have been computed using (wind speed)^2 dependence on the gas transfer rate with wind speeds taken at the 0.995 sigma level (about 40 m above the sea surface). These winds averaged about 1 m s^{-1} faster than the 10 m winds, which should have been used. The flux values updated with 10 m winds are reduced by about 30%, and are available from T. Takahashi at [http://www.ldeo.columbia.edu/res/pi/CO2/carbondioxide/pages/ air_sea_flux_rev1.html].

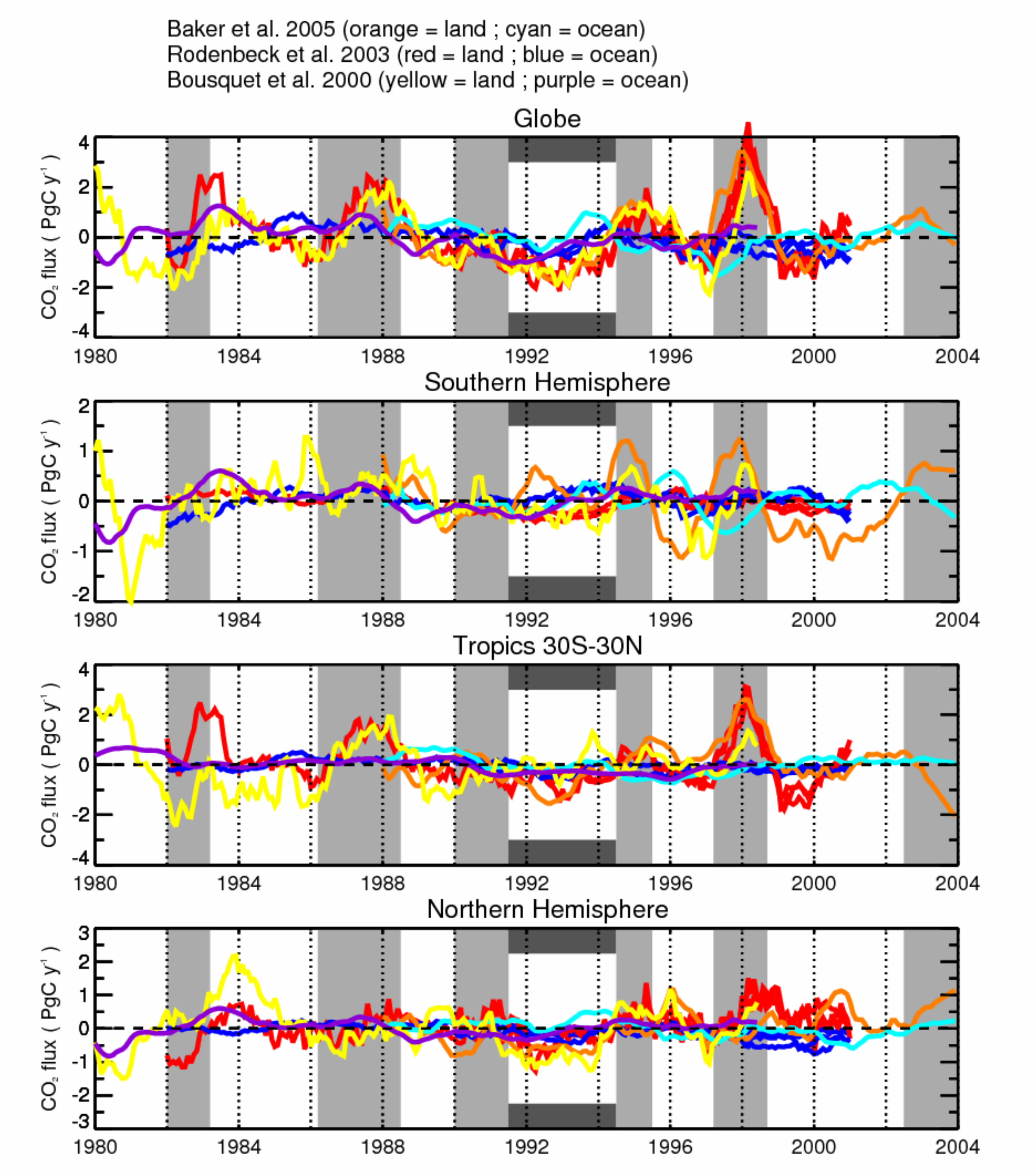

Figure 7.3.8. Ocean-atmosphere and land-atmosphere CO_2 fluxes year-to-year anomalies in GtC yr^{-1}, from interannual inversions ensembles covering the past 20 years or so, grouped into large latitude bands, and over the globe. Three different inversion ensembles from Bousquet, et al. (2000), Rödenbeck, et al. (2003a), and Baker et al. (2005) are shown. For each flux and each region, the anomalies were obtained by substracting the long-term mean flux and removing the seasonal signal.

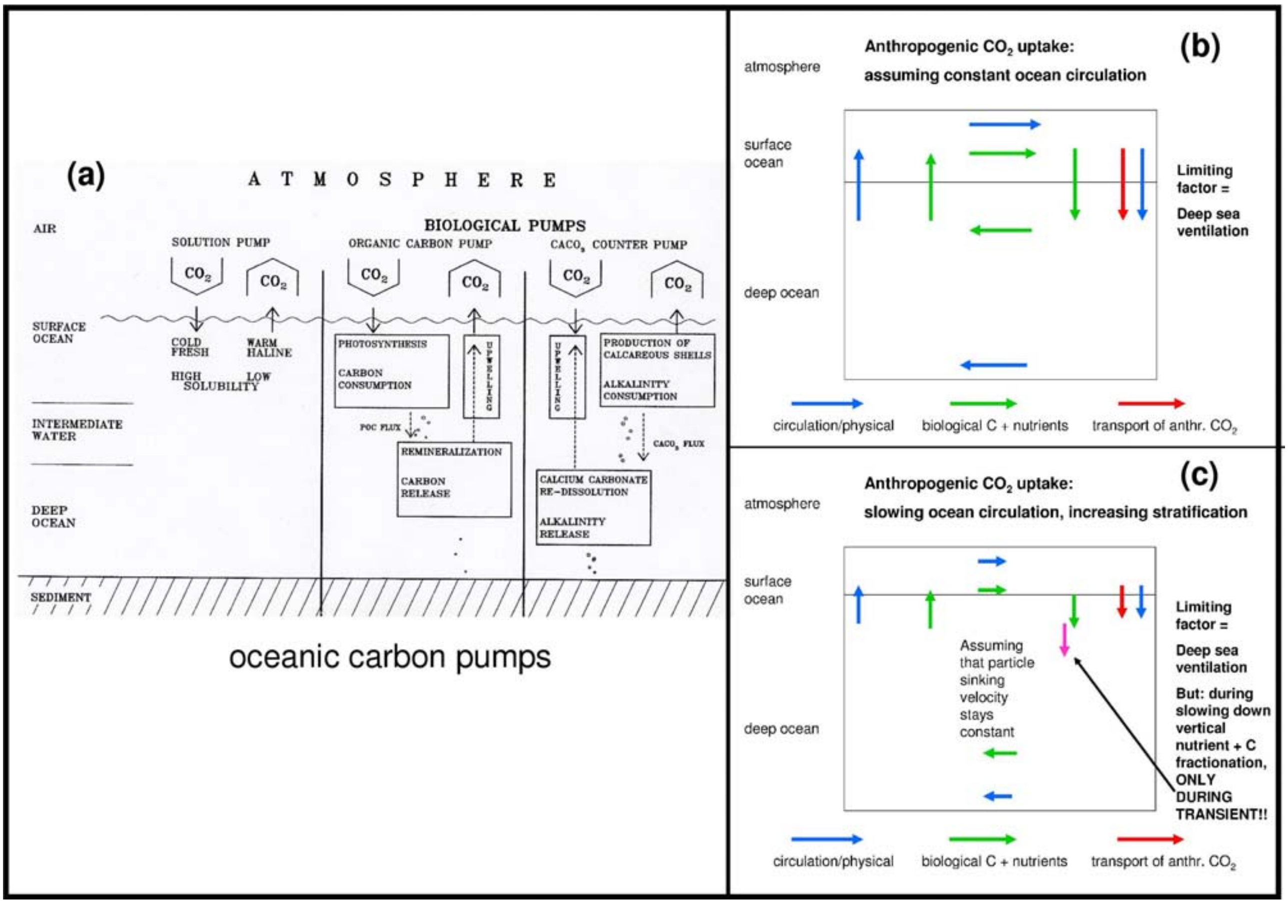

Figure 7.3.9. Panels: (a) Three main ocean carbon pumps govern the regulation of natural atmospheric CO_2 changes by the ocean (Source: Heinze et al., 1991); (b) The oceanic uptake of anthropogenic CO_2 is dominated by inorganic carbon uptake at the ocean surface and physical transport of anthropogenic carbon from the surface to deeper layers ("oceanic bottleneck"). For a constant ocean circulation, to first order, the biological carbon pumps remain unaffected because the nutrient cycling is not changed significantly by these processes; and (c) If the ocean circulation slows down, anthropogenic carbon uptake is dominated by inorganic buffering and physical transport as before. During the slowing down, the marine particle flux can shift somewhat to greater depths if the sinking velocity of the particles does not change. This leads to a biologically-induced negative feedback. This, however, is expected to be smaller than the positive feedback associated with a slower physical downward mixing of anthropogenic carbon.

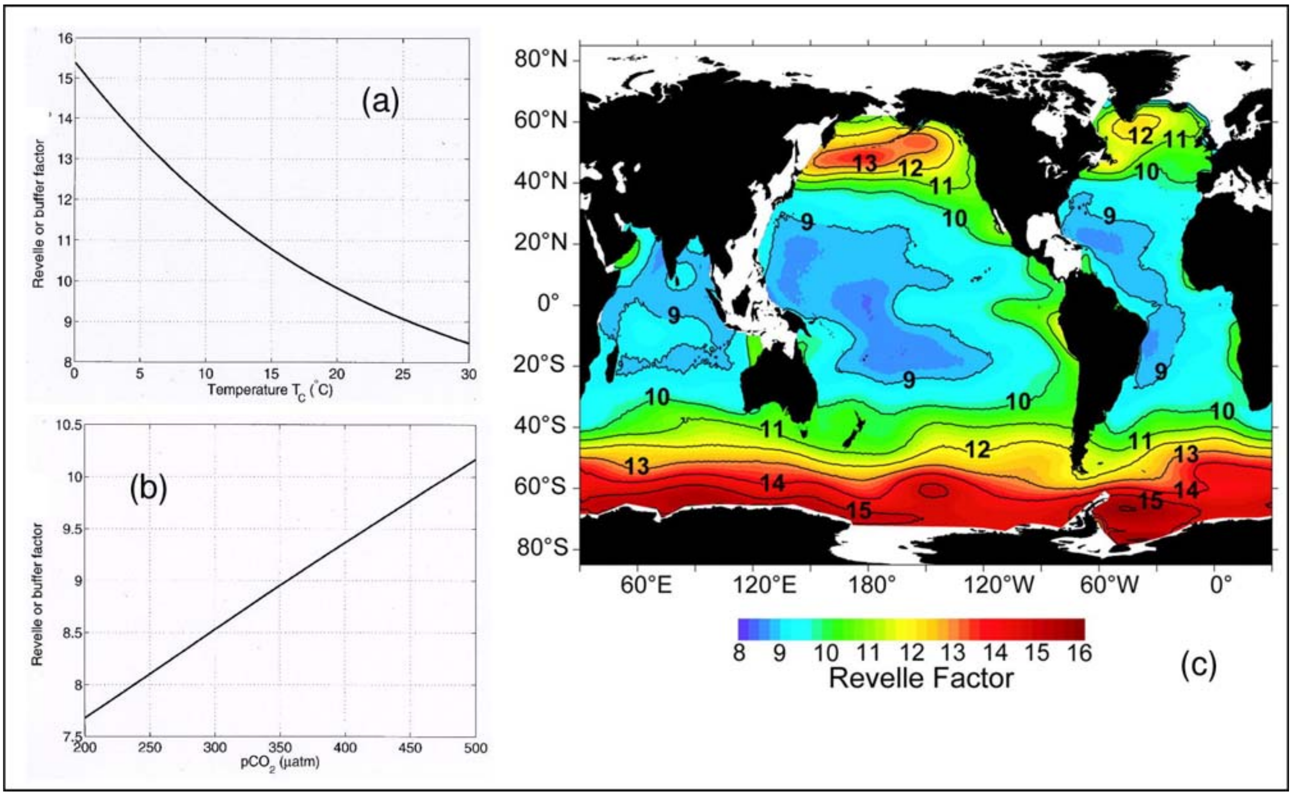

Figure 7.3.10. The Revelle factor (or buffer factor) as a function of seawater temperature (S=35, pCO_2=230 µatm, Talk=2300 µmol kg^{-1}) (a), as a function of pCO_2 (T_C = 25º, S = 35, TAlk = 2300 µmol kg^{-1}) (b), and with its geographical distribution for year 1994 (c). With increasing partial pressure of CO_2 and decreasing temperature, the Revelle factor increases and thus the buffering capacity of the seawater decreases. Source: (a) and (b) from Zeebe and Wolf-Gladrow (2001), (c) from Sabine et al. (2004a).

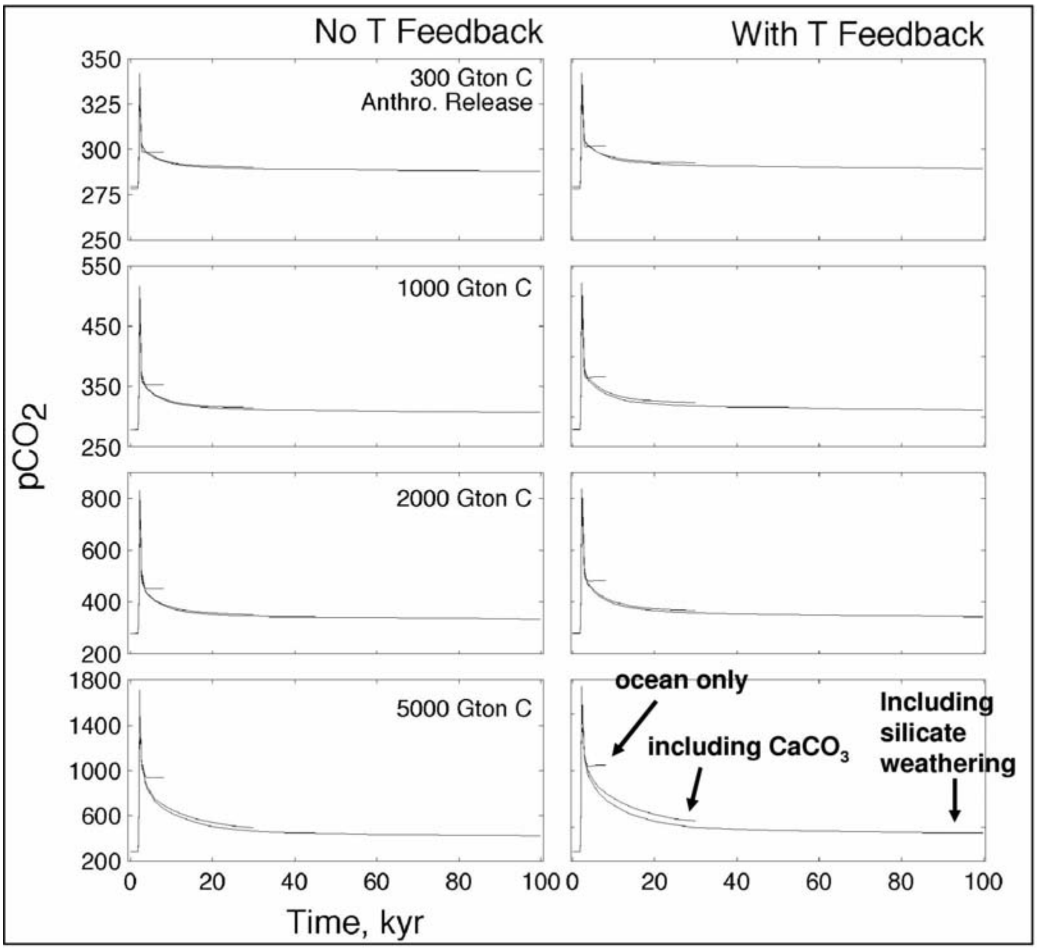

Figure 7.3.11. Model projections for the neutralization of anthropogenic CO_2 to year 100,000 A.D. All panels show atmospheric CO_2 partial pressure (in ppm) time series. Left panel: neglecting ocean temperature feedback. Right panel: including ocean temperature feedback. The ocean only runs go to 9 k yr, $CaCO_3$ equilibrium runs go to 35 k yr, and silicate weathering runs go to 100 k yr (see arrows as examples). From top to bottom, the scenarios are for total anthropogenic CO_2 releases of 300, 1000, 2000, and 5000 GtC. Without $CaCO_3$ dissolution from the seafloor the buffering of anthropogenic CO_2 is limited. Even after 100 kyr, the remaining CO_2 partial pressure is substantially higher than the preindustrial value. Due to the slow decrease of atmospheric CO_2 towards long time scales (the long end of the "tail" at the right side of the diagrams), mean atmospheric lifetimes of anthropogenic CO_2 in the atmosphere amount to 30,000–35,000 years. Source: Archer (2005).

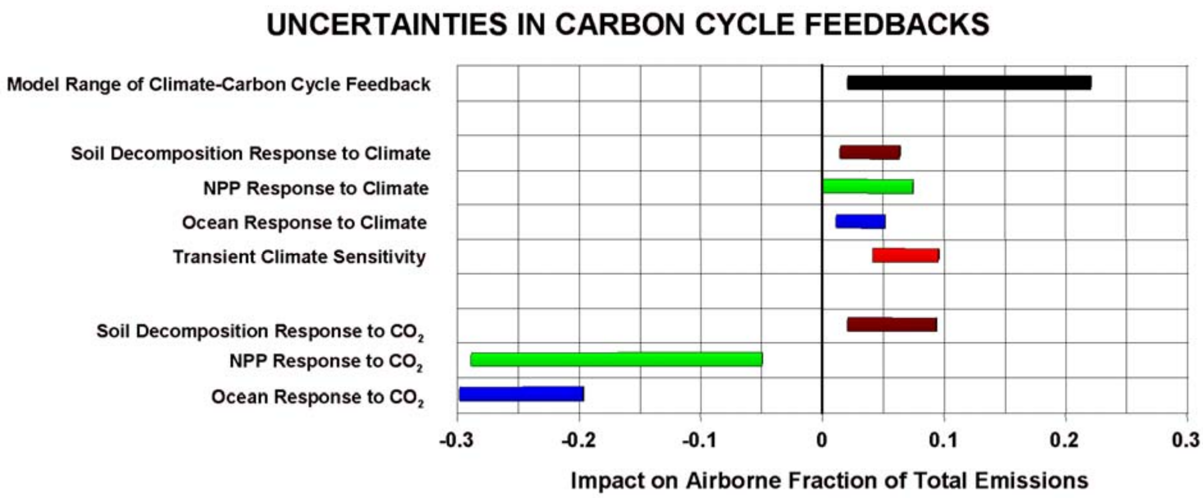

Figure 7.3.12. Uncertainties in carbon cycle feedbacks estimated from analysis of the results from the C^4MIP models. Each effect is given in terms of its impact on the mean airborne fraction over the period 1850–2100, with bars showing the uncertainty range based on the ranges of effective sensitivity parameters given in Tables 7.3.5 and 7.3.6. The lower 3 bars are direct response to carbon dioxide increase (see Section 7.3.5 for details), the middle 4 bars show impacts of climate change on the carbon cycle, and the top black bar shows the range of climate-carbon cycle feedbacks given by the C^4MIP models.

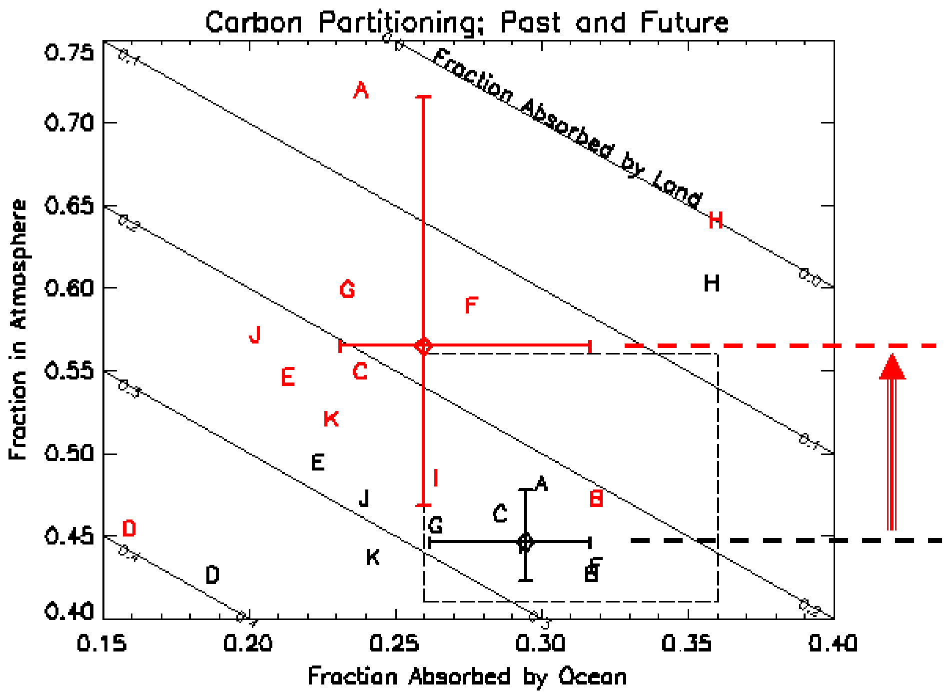

Figure 7.3.13. Changes in the mean partitioning of emissions as simulated by the C^4MIP models up to 2000 (black symbols) and for the entire simulation period to 2100 (red symbols). The symbols represent the models as given in Table 7.3.4. The box shown by the dotted line is a constraint on the historical carbon balance based on records of atmospheric CO_2 increase, and estimates of total emissions (fossil fuel plus land-use emissions) and the oceanic uptake of anthropogenic CO_2 (Sabine et al., 2004a). The black and red crosses show the means and ranges of carbon partitioning simulated by the six C^4MIP models that fit within these constraints. The large red arrow shows the mean tendency towards increasing airborne fraction through the 21st century, which is common to all models.